Molecular Cell, Vol. 19, 595–605, September 2, 2005, Copyright ©2005 by Elsevier Inc. DOI 10.1016/j.molcel.2005.07.015

The Structural Basis of Myosin V Processive Movement as Revealed by Electron Cryomicroscopy

Niels Volkmann,[1] HongJun Liu,[1] Larnele Hazelwood,[1] Elena B. Krementsova,[2] Susan Lowey,[2] Kathleen M. Trybus,[2,*] and Dorit Hanein[1,*]

[1]The Program of Cell Adhesion
The Burnham Institute
La Jolla, California 92037

[2]Department of Molecular Physiology and Biophysics
University of Vermont
Burlington, Vermont 05405

Summary

The processive motor myosin V has a relatively high affinity for actin in the presence of ATP and, thus, offers the unique opportunity to visualize some of the weaker, hitherto inaccessible, actin bound states of the ATPase cycle. Here, electron cryomicroscopy together with computer-based docking of crystal structures into three-dimensional (3D) reconstructions provide the atomic models of myosin V in both weak and strong actin bound states. One structure shows that ATP binding opens the long cleft dividing the actin binding region of the motor domain, thus destroying the strong binding actomyosin interface while rearranging loop 2 as a tether. Nucleotide analogs showed a second new state in which the lever arm points upward, in a prepower-stroke configuration (lever arm up) bound to actin before phosphate release. Our findings reveal how the structural elements of myosin V work together to allow myosin V to step along actin for multiple ATPase cycles without dissociating.

Introduction

The basic mechanism by which all myosins interact with actin is generally conserved, but different myosins have tuned their structural, kinetic, and mechanical properties to optimize performance for their particular cellular role. Myosin V has evolved to spend most of its cycle time attached to actin (i.e., a high-duty cycle), a requirement for it to move processively along an actin filament as it transports cargo (reviewed in Vale, 2003). Myosin V has also undergone structural adaptations to its lever arm, which is elongated and contains six IQ motifs that each binds one calmodulin. This large span between motor domains allows the two heads to bind approximately 36 nm apart from each other as the molecule strides along an actin track for multiple ATPase cycles before detachment. However, the detailed structural mechanism that underlies such processive movement is still not understood.

The only actin bound myosin states that have been amenable to investigation by 3D electron cryomicroscopy to date are "strongly bound" states, i.e., heads with bound ADP or heads without nucleotide (apo), which represent the final steps in the ATPase cycle. These studies showed that the lever arm is in the postpower-stroke position (lever arm down) when myosin is strongly bound to actin and that additional downward movement can occur for some myosins upon ADP release (Volkmann and Hanein, 2000; Whittaker et al., 1995). We previously showed that the large cleft that divides the actin binding region of the motor domain is tightly closed in the rigor state for both smooth and skeletal myosins (Volkmann et al., 2000, 2003). In addition, we have shown that loops at the actin interface (loop 2) and at the nucleotide binding pocket (loop 1) are both flexible and therefore not visible in the crystal structures and become stabilized by actin binding (Volkmann et al., 2000, 2003). Recently, Holmes et al. (2003) have confirmed our observation for a closed actin binding cleft by using a rigor map of skeletal myosin.

Prior electron microscopy studies on myosin V, using negative staining and two-dimensional image averaging, have shown the molecule spanning the ~36 nm actin helical repeat during ATP hydrolysis (Burgess et al., 2002; Walker et al., 2000). Two types of lever arm positions that resemble the crystallographic pre- and postpower-stroke conformations were observed in projection, but no high-resolution information on changes within the motor domain could be obtained.

The only atomic-resolution myosin V structures available to date are in detached states, either without nucleotide (Coureux et al., 2003) or in the presence of ADP or ADP.BeF_x (Coureux et al., 2004). The nucleotide-free structure captures a unique conformation in which the lever arm is in a downward position, the actin binding cleft is in a closed conformation, and specific interactions between elements at the active site prevent high-affinity nucleotide binding. The structure in the presence of ADP was obtained by soaking preformed nucleotide-free crystals with ADP, resulting in minimal alterations of the nucleotide-free structure. Thus, this structure is believed to represent an intermediate state in which ADP is bound weakly to myosin and confirms that a closed cleft geometry is compatible with ADP binding (Coureux et al., 2004). The structure of myosin V in the presence of ADP.BeF_x is similar to the postpower-stroke structures of myosin II (Fisher et al., 1995; Gulick et al., 1997; Rayment et al., 1993b) that are characterized by an open cleft and a downward lever arm position. These atomic myosin V structures provide detailed information about changes within the detached myosin head, but corresponding changes in actin and at the actomyosin interface can only be deduced by studying actin bound myosin.

Here, we use electron cryomicroscopy (cryoEM) to visualize actin bound structures of an expressed monomeric murine myosin V construct containing the motor domain and two calmodulin binding IQ motifs (MD2IQ). Myosin V's relatively high affinity for actin in the presence of ATP and triphosphate analogs allows us to visualize previously inaccessible states. Thus, 3D recon-

*Correspondence: trybus@physiology.med.uvm.edu (K.M.T.); dorit@burnham.org (D.H.)

Table 1. Reconstruction Quality Indicators

	ADP	Apo	ATP	AMPPNP[d]	ADP.AlF$_4$
Units in average[a]	5485	5044	5308	11006	8411
Phase residual[b]	23°	22°	25°	n/a	n/a
Units per turn	2.157 ± 0.002	2.158 ± 0.002	2.159 ± 0.003	2.156 ± 0.005	2.161 ± 0.007
Resolution (nm)	2.10	2.10	2.10	4.22 ± 0.31	5.43 ± 0.42
Docking accuracy [c] (nm)	0.26	0.24	0.34	0.98	n/a

[a] Units for the nucleotide states are corrected for repeated use of the same units.
[b] Calculated from the contributing filaments, there is no analogy for iterative helical real space refinement.
[c] No docking was performed for the ADP.AlF$_4$ state.
[d] AMMPNP refers to prepower-stroke map after sorting.

structions were obtained of the actin-MD2IQ complex in the presence of ATP, AMPPNP, ADP.AlF$_4$, ADP, and in the nucleotide-free state, structures that should mimic the normal progression through the hydrolysis cycle. We show that ATP weakens actin binding by opening the long cleft dividing the motor domain while rearranging loop 2 as a tether. The presence of AMPPNP or ADP.AlF$_4$ induces a conformational state with the lever arm pointing in a prepower-stroke upwards configuration. The actin bound nucleotide-free and ADP structures, similar to the detached crystal structures, have their cleft tightly closed with the lever arm pointing downwards.

Results

Reconstructions of Actin Decorated with Myosin V in the Strong Binding States (ADP, apo) and in the Presence of ATP Show Postpower-Stroke Lever-Arm Conformations

Electron cryomicroscopy and helical reconstruction techniques were used to generate 3D maps for actin filaments as well as for myosin V MD2IQ-decorated actin filaments in the absence of nucleotide and in the presence of ADP or ATP (see Table 1 for quality indicators). We also processed each data set by using the iterative helical real space refinement method (Egelman, 2000). The resulting reconstructions were very similar (correlation >95%) to the respective helical reconstructions. All three nucleotide states show the lever arm in postpower-stroke position, similar to those obtained for actin bound myosin II (Holmes et al., 2003; Rayment et al., 1993a; Volkmann et al., 2000, 2003; Whittaker et al., 1995) (Figure 1).

Acto-myosin V incubated with ATP could result in a mixed population of the true ATP state and various intermediate states. To ensure that our reconstructions of actin bound myosin V in the presence of ATP represent homogeneous populations, we carefully analyzed the appearance and optical diffraction patterns of filaments before we selected them for averaging. Inhomogeneity would be immediately apparent in the images as well as the diffraction patterns and would also affect the averaging statistics adversely. All filaments included in the average appeared homogenous, and the averaging statistics of the selected filaments support this notion in that its quality is comparable to those of the strongly bound states (see also Table 1).

To further test for mixed conformations in the resulting reconstruction, we determined the Absolute Values of Individual Differences (AVID) for these maps. The AVID procedure was specifically developed to identify mixtures of states and conformations in helical reconstructions (Rost et al., 1998). Because the AVID maps of the ATP state are virtually featureless (all values were less than one standard deviation away from the mean), there is no significant structural variability or mixture present in the ATP reconstructions. We also checked the density distribution of the reconstructions for signs of mixed populations, which would change the relative strength of features in the maps. Regions of the underlying structure that are not well locked into space would spread their density over a larger area and would appear weaker than well-determined entities (see the Supplemental Data available with this article online). In the reconstructions done in the presence of ATP, the relative strength of actin, the motor domain, and the light chains are comparable to those of the apo and ADP maps. We conclude that the reconstructions obtained in the presence of ATP represent homogenous populations of a state that is significantly different from the ADP state (see below). We will refer to this state as the "ATP state."

Docking Analysis Indicates a 2.4 nm Lever-Arm Movement upon ADP Release

An atomic model for filamentous actin (see Experimental Procedures for details) was docked into maps of undecorated actin. The accuracy of the docking in this region was estimated at 0.18 nm. Modular docking (Volkmann and Hanein, 1999) of multiple crystal structures was performed on single asymmetric units of the respective actin bound myosin-V densities to obtain atomic models for the apo, ADP, and ATP actin bound myosin V (254 docking experiments). To compile the statistics, the available crystal structures were divided into three different groups corresponding to the prestroke (lever arm up), poststroke (open cleft and lever arm down), and closed-cleft (lever arm down) conformations (see Supplemental Data for details). The correlation statistics (Table S1) show that for all three reconstructions, the prepower-stroke group fits significantly less well than the other two groups when the converter is present. If the converter is deleted, there is no difference among the three groups. The analysis of the solution sets results in estimated docking accuracies for the MD region of 0.24 nm, 0.26 nm, and 0.34 nm for the apo, ADP, and ATP maps, respectively.

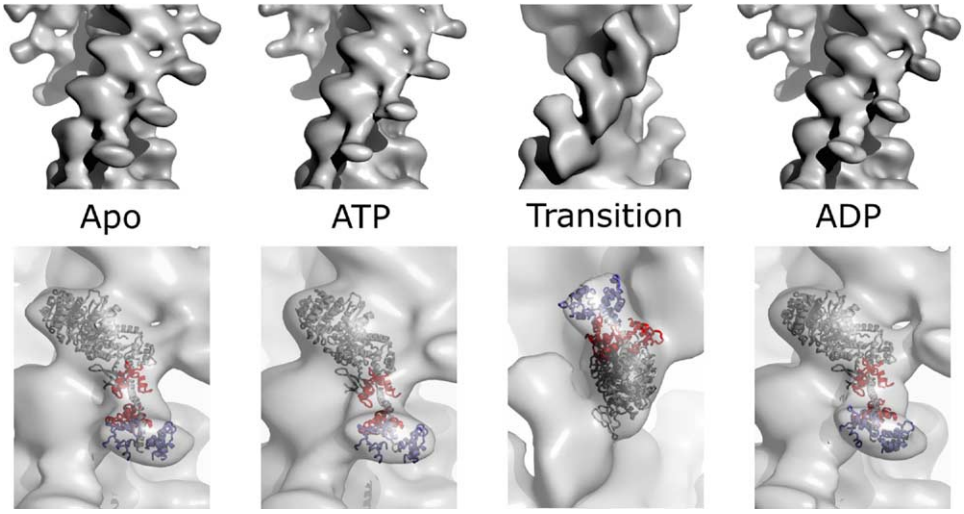

Figure 1. 3D Reconstructions of Actin Filaments Decorated with Myosin V in the Presence of Various Nucleotides (Gray Surface Representations)

The pointed end of actin is toward the top of the figure, and the direction of movement points downwards. Docked myosin structures are shown in cartoon representation. The motor domain is in gray and the two bound calmodulins are in red and blue. The strongly bound states as well as the ATP state show the lever in the postpower stroke, downward position, pointing in the direction of movement. In the presence of AMPPNP or ADP.AlF_4, the lever arm points upwards, poised for the postulated prepower stroke. See also Movies S1–S4.

The subsequent docking of the calmodulin chains rotates the first calmodulin by 25 ± 5° with respect to the detached myosin V apo crystal structure (Coureux et al., 2003), resulting in a displacement of ~1 nm for all three maps. Although the lack of spatial constraints in the region of the second calmodulin makes determination of the orientation highly ambiguous, the center of mass is reproducibly in the same spot within 0.4 nm. A t-test analysis of the calmodulin center of mass distributions shows that there is a small but statistically significant ($p = 0.005$) change of lever-arm position when ADP is released. This change translates into an angular swing of ~6° from the ADP to the apo state, corresponding to an ~2.4 nm translation extrapolated to the end of the full-length lever arm. There is no significant change between the apo and ATP states in this regard.

Actin Bound Myosin V in the Presence of AMPPNP or ADP.AlF_4 Represents a Prepower-Stroke Transition State

Standard helical reconstructions of actin decorated with MD2IQ in the presence of the nucleotide analogs AMPPNP or ADP.AlF_4 did not show a single lever-arm position but appeared to contain a mixture of two different states. The data were reprocessed with a new implementation of the iterative helical real space refinement. In contrast to standard helical reconstruction methods, this approach can resolve and sort mixtures of conformations (Galkin et al., 2001; Lukoyanova et al., 2002; Yang et al., 2003) and can retrieve 3D structures even from poorly ordered helices (Galkin et al., 2003a). The application of this method to the AMPPNP and ADP.AlF_4 data (see Supplemental Data for details) resulted in reconstructions that both showed the same morphology: the actin filament and the motor domain were clearly visible and, in addition, two densities emerged from the motor domain (see Figure S1A in the Supplemental Data available with this article online). One density was in a position similar to that of the lever arm seen in the reconstructions in the presence of ATP and the other density protruded upwards, similar in position to the lever arm modeled from the crystallographic transition state. According to the Fourier shell correlation (FSC), there is no significant difference between the AMPPNP and ADP.AlF_4 reconstructions at the resolution of the latter (FSC greater then 0.5), indicating that they represent similar structural states within the hydrolysis cycle.

To separate the two conformations in the AMPPNP data, we employed multireference alignment with calculated model densities representing prepower-stroke and postpower-stroke actomyosin structures (see Supplemental Data for details). Similar reference-based sorting strategies have been used extensively and successfully on actin-filament structures with much less distinct differences (Galkin et al., 2001, 2002, 2003b; Lukoyanova et al., 2002; Orlova et al., 2004; Yang et al., 2003). The reconstructions with segments that were sorted into the prepower-stroke model classes consistently converged to a structure with only a single density emerging, similar in position to that of the prepower-stroke model (Figure 1, "transition"). FSC calculations between reconstructions from different starting models indicated a resolution of 4.22 (±0.31) nm when using the 0.5 cutoff criterion. It should be noted that the resulting reconstruction is significantly different from the starting model, both in motor domain attachment and lever-arm angle (see below). The reconstruction resulting from the segments that were sorted into the postpower-stroke classes has an appearance similar to the ATP or strong binding state maps (lever arm downwards, Figure S1B)

with a resolution of 4.04 ± 0.26 nm (from FSC 0.5 cutoff). The ADP.AlF_4 data set exhibited a much higher background and a significantly worse signal-to-noise ratio than the AMPPNP data set. As a consequence, no stable reconstruction could be obtained for the ADP.AlF_4 data set after sorting (see Supplemental Data).

Owing to the relatively low resolution of the AMPPNP reconstructions, we could not use the modular docking strategy for the modeling of the AMPPNP state and instead followed an iterative refinement protocol (see Supplemental Data for details). The resulting estimated accuracy of the docking within the MD is 0.98 nm. The orientations of the calmodulins are not well determined, but their center of mass positions are reproducible within 0.4 nm. By using the position of G697 as a pivot point and the center of mass of the second calmodulin as the moving entity, an angular swing of ~105 ± 5° parallel to the actin filament axis from the AMPPNP to the ADP occurs that, extrapolated to the full length of the lever arm, corresponds to a 36.8 ± 1.2 nm translation at the end of the lever arm for the transition from AMPPNP to ADP.

The Actin Binding Cleft Is Closed Tightly in the apo and ADP States and Opens in the Presence of ATP

More subtle structural changes in the myosin V motor domain induced by actin and nucleotide binding were characterized by our previously developed discrepancy mapping technique (Volkmann et al., 2000). Briefly, atomic models for the bound states are first created by computer-based fitting of myosin crystal structures into the 3D reconstructions. The density calculated for the fitted models is corrected for the characteristic resolution falloff and contrast transfer effects in the data and then is subtracted from the 3D reconstruction. "Discrepancy peaks," which emerge from this analysis, identify regions of higher density in the reconstructions that are not accounted for by the atomic models (Figure 2). We showed previously that a resolution of 2.5 nm is sufficient for monitoring the amount of cleft closure for myosin II through discrepancy mapping (Volkmann et al., 2003). This finding was reconfirmed by docking the myosin V open-cleft ADP.BeF_x crystal structure (Coureux et al., 2004) into a 2.5 nm resolution map calculated from the myosin V closed-cleft crystal structure (Coureux et al., 2003), resulting in a discrepancy map that clearly shows a peak in the cleft region (Figure S2).

For the experimental reconstructions, there were statistically significant peaks in the actin binding cleft region of the apo and ADP states for discrepancy maps of all post- and prestroke structures, indicating that the cleft is closed more tightly than in those crystal structures. These peaks disappeared when the closed-cleft myosin V structures were used for the calculations. In the ATP state, there was no extra density in the cleft region, no matter which crystal structure was used, even if the significance criterion was substantially relaxed. The lack of extra density in the cleft region shows clearly that the actin binding cleft in the ATP state is open.

Loop 2 of Myosin V Acts as a Tether for the Weakly Bound States

Our discrepancy map analysis shows significant peaks in the vicinity of loop 1 (near the entrance of the nucleotide binding pocket) and loop 2 (the charged loop at the actin binding interface) for all three states (Figures 2 and 3). These loops are disordered in the detached crystal structures, and the presence of extra density in the actomyosin reconstructions indicates that these loops are stabilized upon actin binding. We confirmed by test calculations that changes in stability and position of loop 1 and loop 2 can explain all the observed discrepancy map patterns at the resolution of the reconstructions (details in the Supplemental Data and Figure S2). In the presence of ATP, the loop 2 density shows a clear and significant shift from the position it adopts in the strongly bound states. Loop 2 moves away from acidic residues in subdomain 1 of actin (near the N terminus and residues 24–28), and extends toward subdomain 2 of the actin monomer below. The loop rearranges again in the presence of AMPPNP and interacts electrostatically with the N-terminal acidic patches of the upper actin and with an acidic patch around residue 100 of the lower actin. Thus, loop 2 maintains contact in the weakly bound states of myosin V and tethers the molecule to the actin filament.

Actomyosin Interactions Change Substantially During the Hydrolysis Cycle

The solution-set approach used for docking in this study allows assigning of the probability of interaction to each atom of the interaction partners (Volkmann et al., 2000). Briefly, for all solutions that are part of the solution set (i.e., are compatible with the data), the distance for each atom to the interface is tested. If the atom is closer than the interaction distance (0.6 nm in this study), the atom gets a score of one and otherwise is assigned as zero (Hanein et al., 1998). The scores are added up for all permissible solutions and divided by the number of solutions used for the calculation. The higher the score, the more consistently the atom is within the interaction distance of its binding partner.

Figures 4 and 5 show how the interaction probabilities develop during the hydrolysis cycle. In the presence of ADP, the main areas of interaction are very similar to those of smooth muscle and skeletal myosin II (Volkmann et al., 2000, 2003). These regions include the helix-turn-helix motif (residues 492–533) and the secondary actin binding loop (540–546) in the lower 50 kDa domain, the cardiomyopathy loop (376–392) in the upper 50 kDa domain, and the vicinity of loop 2 (592–634). In addition, a loop protruding from the upper 50 kDa domain (340–350) displays some interaction probability. There is little change between the ADP and apo states. Upon ATP binding, the interaction is weakened in the upper 50 kDa domain and there is a slight shift in binding in the lower 50 kDa domain. In the presence of AMPPNP, all the interactions in the lower 50 kDa domain are abandoned and only a slight possibility for electrostatic interactions of K517 with the region around E99 and E100 in the lower monomer remains in this area. Also, the cardiomyopathy loop, the 340–350 loop, and a previously noninteracting, positively charged patch around two helices in the upper 50 kDa domain (D367–E375 and 574–580) display some but relatively weak interaction probabilities in the AMPPNP state. Whereas the cardiomyopathy loop contacts the upper actin monomer in the other three states, it appears close to sub-

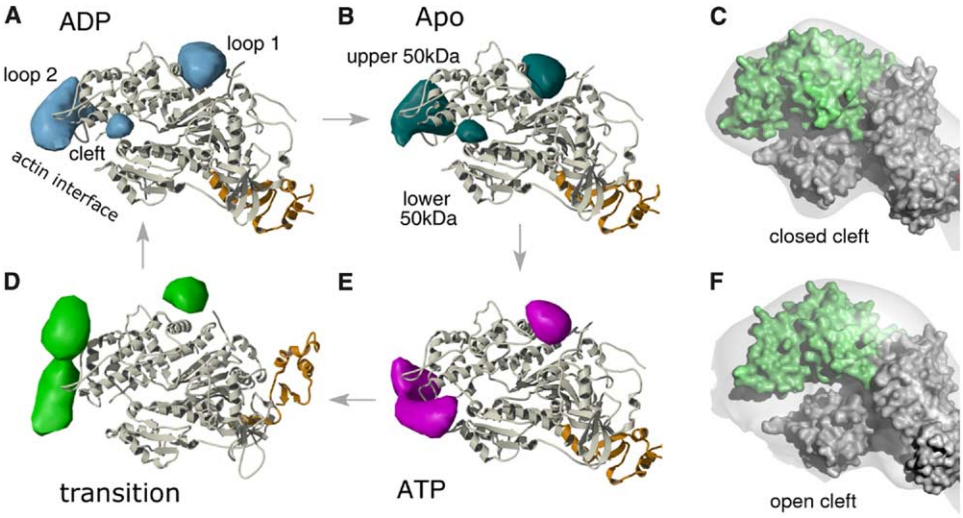

Figure 2. Nucleotide-Dependent Changes within the Myosin V Motor Domain

Only residues up to the start of the lever arm are shown in cartoon representation. The converter domain (residues 697–754) is shown in orange. Discrepancy peaks, representing density in the reconstructions that the docked models do not account for, are shown as surface representations. There are peaks close to the resolved ends of loop 1 and loop 2 in all four nucleotide states, indicating that these loops are ordered in all actin bound states. Whereas loop 1 does not change shape or position, loop 2 changes substantially in the weakly bound states (D and E). Structures with an open cleft were used to calculate all discrepancy maps. The peaks in the cleft of the strongly bound states (A and B) indicate that the cleft is more closed than in the crystal structures (Volkmann et al., 2000, 2003). These peaks disappear if the myosin V crystal structure with closed cleft geometry (Coureux et al., 2003) is used. There is no peak in the cleft of the ATP state (E) for any of the crystal structures, including those with an open cleft. The relatively low resolution of the transition state reconstructions did not allow the degree of cleft closure to be determined for this state (see also Figure S2). Solvent-exposed surface representations of the open and closed cleft states are shown in (C) and (F), respectively. The upper 50 kDa domain is shown in light green. Orientation is as in (B) and (E), respectively.

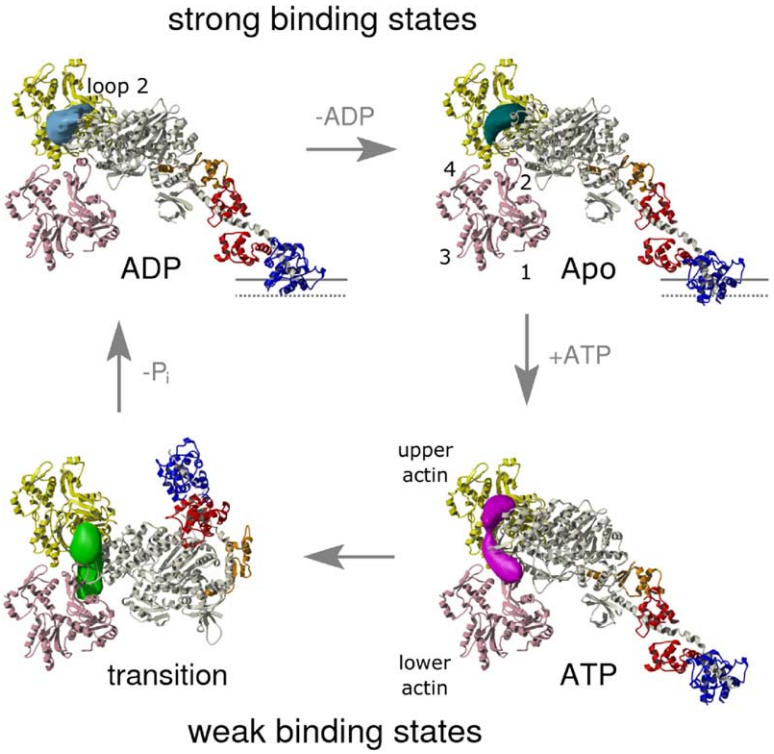

Figure 3. The Structural Changes During the Myosin V ATPase Cycle

Two actin monomers (upper monomer in yellow, lower monomer in pink), the attached myosin motor domain (gray), and the two bound calmodulins (red and blue) are shown in cartoon representation. Converter (residues 697–754) is shown in orange. The pointed end of the filament is toward the top of the figure, and the direction of movement is downwards. The discrepancy peaks representing loop 2 are shown as surface representations. The solid and dashed lines highlight movement of the lever arm upon ADP release (see Supplemental Data for details).

Residue	ADP	Apo	ATP	AMPPNP	*Residue*	ADP	Apo	ATP	AMPPNP
	Protruding Loop in Upper 50 kD Domain								
R343	0.19	–	–	0.42	*D344*	1.00	–	–	0.75
S345	1.00	0.83	–	0.69	*D346*	0.72	–	–	0.52
	Cardiomyopathy Loop, Upper 50 kD Domain								
R378	0.68	0.33	–	0.15	*K379*	0.92	0.97	–	0.33
L380	1.00	1.00	0.46	0.27	*A381*	1.00	1.00	0.81	0.21
T386	1.00	1.00	0.68	0.46	*Y387*	1.00	1.00	0.70	0.46
I388	0.96	0.81	–	0.37	*K389*	1.00	1.00	0.49	0.40
	Helix-Turn-Helix Motif, Lower 50 kD Domain								
K502	1.00	1.00	1.00	–	*M503*	1.00	1.00	0.46	–
D507	1.00	0.88	0.51	–	*E511*	1.00	0.97	0.60	–
K515	0.69	0.40	0.75	–	*P516*	0.87	1.00	1.00	–
K517	1.00	0.89	0.82	0.25	*Q525*	0.39	0.23	0.63	–
N529	0.36	0.44	0.81	–	*L532*	–	–	0.53	–
N533	–	–	0.65	–					
	Secondary Actin Binding Loop, Lower 50 kD Domain								
K540	0.20	0.13	0.95	–	*P541*	0.04	–	0.86	–
R542	1.00	1.00	1.00	–	*L543*	1.00	1.00	0.96	–
S544	0.43	0.59	0.98	–	*N545*	0.85	1.00	0.88	0.12
K546	0.40	0.67	0.44	–					
	Actin Binding Loop (Loop 2) Vicinity								
H632	0.97	0.99	0.61	–					
	Extra Helices Interacting in AMPPNP Only, Upper 50 kD Domain								
D367	–	–	–	0.52	*Y368*	–	–	–	0.37
E369	–	–	–	0.44	*E370*	–	–	–	0.48
E575	–	–	–	0.37	*K578*	–	–	–	0.38

Figure 4. Myosin Interaction Probabilities

Only residues with interaction scores of at least 0.37 in at least one of the states are shown. Residues with scores less than 0.1 are denoted (–). Residues are color coded according to their primary interaction partner on myosin. The upper 50 kD protruding loop is shown in blue; the cardiomyopathy loop is in red; the helix-turn-helix motif is in green; the secondary actin binding loop is in magenta; the actin binding loop vicinity is depicted in yellow; and the additional upper 50 kD helices in the AMPPNP state is in gray.

domain two of the lower monomer in this state. The positively charged region that only interacts in the AMPPNP state is close to the N-terminal end of the upper actin monomer.

Discussion

By means of cryo EM reconstructions and computer-based docking of myosin crystal structures into the 3D maps, we have obtained atomic models of actin bound myosin V in the strong binding states (in the presence of ADP and in the absence of nucleotide, i.e., apo) and in the weak binding states (in the presence of ATP and AMPPNP/AlF_4). This approach was used to identify actin and nucleotide-induced changes in the conformation of the motor domain, the actomyosin interface, the actin binding cleft, and the position of the lever arm.

During steady-state hydrolysis of ATP, solution studies indicate that most myosin heads would have ADP bound (De La Cruz et al., 1999). Nonetheless, the cryo EM data clearly show that we have trapped a bound intermediate in the presence of ATP that is not the same as adding ADP. The transition that precedes and limits ATP hydrolysis is very temperature dependent, and the equilibrium constant for hydrolysis is <1 when calmodulin is next to the motor domain (De La Cruz et al., 2000). It is possible that these features contributed to our trapping of a novel actin bound state in the presence of ATP. Our analysis shows that the cleft conformation for myosin V in the actin bound ATP state is unique in being "open" because it did not show any extra density in the cleft region, even when compared to the most open crystal structure (Rayment et al., 1993b). In contrast, there was extra density in the cleft region of myosin V in the ADP and apo states when compared to all crystal structures except for the "closed" myosin V conformation, indicating that the cleft is tightly closed when myosin V is strongly bound to actin (Figure 2). This result implies that cleft opening provides the structural basis by which actomyosin binding is weakened by ATP binding.

Two positions of the lever arm are present within a single filament in the presence of AMPPNP or ADP.AlF_4. One population of heads showed the lever arm in a

Residue	ADP	Apo	ATP	AMPPNP	*Residue*	ADP	Apo	ATP	AMPPNP
	Upper Actin – Subdomain 1 (N-Terminal)								
E5	–	–	–	0.44	*G23*	0.97	0.95	0.33	0.27
D24	0.38	0.13	0.16	0.13	*D25*	0.91	0.89	–	0.17
A26	1.00	0.28	–	–	*P27*	0.83	–	–	–
	Upper Actin – Subdomain 3								
A144	0.56	0.11	0.32	–	*S145*	0.61	0.17	0.60	–
G146	0.93	1.00	1.00	–	*R147*	0.83	0.92	0.96	–
T148	1.00	1.00	0.98	–	*T149*	0.76	0.11	0.67	–
G301	0.47	–	–	–	*T304*	0.29	0.51	–	–
M305	1.00	0.60	–	–	*K326*	0.91	0.40	–	–
K328	1.00	0.84	0.74	–	*I329*	0.33	0.13	0.56	–
I330	0.81	1.00	0.46	–	*A331*	0.75	1.00	0.47	–
P332	1.00	1.00	0.60	–	*P333*	1.00	1.00	0.79	–
E334	1.00	1.00	0.40	–	*R335*	1.00	1.00	0.18	–
	Upper Actin – Subdomain 1 (C-Terminal)								
K336	0.95	0.89	–	–	*Y337*	0.93	0.96	–	–
S338	0.47	0.15	–	–	*I341*	0.96	0.91	–	–
I345	0.71	0.89	0.68	0.33	*S348*	0.73	0.37	0.46	0.44
L349	1.00	1.00	0.81	0.52					
	Lower Actin – Subdomain 1 (N-Terminal)								
L21	–	–	0.60	–	*R28*	–	–	0.44	–
	Lower Actin – Subdomain 2								
K50	0.20	0.31	0.77	0.29	*E57*	–	–	0.46	0.17
	Lower Actin – Subdomain 1 (Central)								
H87	0.60	–	0.68	0.29	*F90*	0.55	0.52	0.39	0.17
Y91	1.00	1.00	0.84	0.33	*N92*	0.85	1.00	0.77	0.31
E93	–	–	0.58	0.13	*L94*	–	0.36	1.00	–
R95	0.68	1.00	1.00	0.23	*V96*	0.89	1.00	0.91	0.10
A97	0.92	1.00	0.42	0.13	*P98*	0.93	0.93	–	0.10
E99	1.00	0.91	–	0.35	*E100*	0.27	0.91	–	0.25

Figure 5. Actin Interaction Probabilities

Only residues with interaction scores of at least 0.37 in at least one of the states are shown, residues with scores less than 0.1 are denoted (–). Residues are color coded according to their primary interaction partner on myosin. The upper 50 kD protruding loop is shown in blue; the cardiomyopathy loop is in red; the helix-turn-helix motif is in green; the secondary actin binding loop is in magenta; the actin binding loop vicinity is depicted in yellow; and the additional upper 50 kD helices in the AMPPNP state is in gray.

postpower-stroke conformation similar to the ATP state, and a second population showed a conformation in which the lever arm had undergone a dramatic upward shift to a position almost parallel to the filament axis and was poised for the postulated "power stroke" (Figure 1, "transition state"). This new conformation of the lever arm is closest to that observed in the crystal structure of smooth muscle myosin with a transition-state analog bound to the active site (Dominguez et al., 1998). Biochemical studies with myosin V suggest that AMPPNP induces a state that is intermediate between weak and strong binding, which could represent a post-hydrolysis ADP.Pi state (Yengo et al., 2002). The angle of the lever arm in this state with respect to the actin filament appears to be larger than that observed in 2D averages of negatively stained two-headed constructs (Burgess et al., 2002). The difference may be due either to the lack of the second head in our construct, which would restrain the movement of the lever arm, or potentially due to artifacts in the negatively stained preparation in the studies of Burgess et al. (2002, 1997). Extrapolating our data to a full-length lever arm, we would predict a maximum change in lever-arm position of 35–38 nm from the transition state to the ADP state, assuming that the lever arm acts as a rigid rod. This extrapolated value is higher than the functional 20–25 nm power stroke determined from optical trap measurements of single-headed constructs (discussed in Moore et al., 2004), implying that compliancy in the lever arm may contribute to decreasing the effective working stroke.

In the strongly bound myosin V states, the lever arm is in a postpower-stroke position, pointing toward the direction of movement and corresponding to the "downward" position in reconstructions of various myosin IIs (Holmes et al., 2003; Rayment et al., 1993a; Volkmann et al., 2000, 2003; Whittaker et al., 1995) (Figure 1, ADP and apo). ADP release in myosin V causes an additional

rotation of the lever arm of approximately 6° toward the walking direction, resulting in an extrapolated extra step of 2.4 nm for the end of the full-length lever arm. In the presence of ATP, the lever arm position does not change appreciably from that observed in the apo state.

The docking analysis also clearly shows that in addition to the changes in the light-chain region, there is a major change in the orientation of the motor domain as the cycle progresses (see Figures 4 and 5), consistent with results from tomograms of insect flight muscle (Taylor et al., 1999). In the strongly bound states, the binding involves hydrophobic contacts between the lower 50 kDa domain and actin similar to those found for myosin II (Figure 3) (Milligan, 1996; Volkmann et al., 2000). This contact is completely abandoned in the actin bound transition state. Instead, a number of interactions between charged surface patches are formed, including the N terminus of the upper actin with the area around residue E370 in myosin V and between subdomain 1 of the lower actin (around residue R95) and the protruding loop around R343. Thus, the actin binding interface is completely altered in this conformation and appears to be dominated by electrostatic interactions.

A positively charged surface loop at the actin binding region (loop 2) adopts an ordered conformation when myosin V is strongly bound to actin, similar to what is seen with myosin II (Volkmann et al., 2000, 2003) (Figures 2 and 3). This loop rearranges significantly in the bound ATP state and again rearranges in the bound transition state. In the presence of ATP, loop 2 moves away from acidic residues in subdomain 1 of actin and extends toward subdomain 2 of the actin monomer below (Figure 3). Loop 2 of myosin V thus "tethers" actin in the presence of ATP, allowing myosin to stay attached even though the strong binding interface is disrupted by opening of the cleft. In the bound transition state, loop 2 interacts electrostatically with acidic patches of both the upper and the lower actin. This idea is consistent with mutational studies that show that the positive charge of loop 2 dictates its affinity for actin in the presence of ATP (Joel et al., 2003; Yengo and Sweeney, 2004).

Our data reveal structural insights that allow us to add information to the current consensus model of processive movement of double-headed myosin V on actin (Figure 6) (reviewed in Vale, 2003). We start arbitrarily with a configuration in which the trailing head is strongly attached to actin in the ADP state and the leading head is detached and in the ADP.Pi conformation (Figure 6A). The trailing head has its lever arm in a nearly postpower-stroke configuration (i.e., its lever arm points downward in the walking direction), and the cleft is closed. The leading head is detached and in the ADP.Pi conformation with the lever arm in a prepower-stroke conformation, searching for the next actin binding site. The leading head binds to actin primarily through electrostatic interactions between loop 2 and acidic patches in both the upper and lower actins (Figures 6A and 6B). Thus, loop 2 acts as a tether, which allows the head to maintain attachment when it is not under strain (i.e., it did not release Pi yet). Actin binding triggers Pi release from the leading head. When the Pi is released, the energy is stored in the strained head,

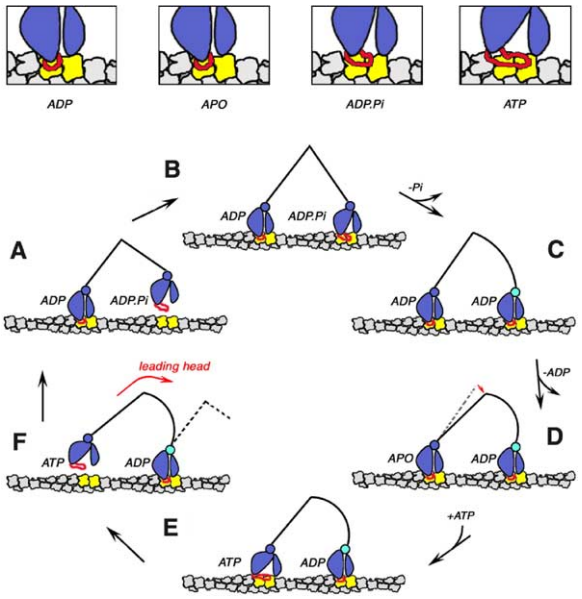

Figure 6. Model for the ATPase-Driven Processive Movement of Double-Headed Myosin V on F-Actin, Incorporating the Structural Insights from the Strongly and Weakly Bound Myosin V States Characterized in This Study

The upper row shows schematic drawings of the actomyosin interface and the associated changes in loop 2 (red) and the actin binding cleft of myosin (see text for details). Only the actin binding region of myosin V is shown here (in blue). The two interacting actin monomers are shown in yellow, the rest of the filament is shown in gray. (A)–(F) show how these structural states fit into the current model of myosin V processive movement. Here, the myosin molecules (blue) are stylized as the upper and lower 50 kDa domains and the converter (circle). The relative orientation between the upper and lower 50 kDa domains determines the closure state of the cleft. The two lever arms that each bind six calmodulins are shown as black lines; strain is depicted as arcs and with a light blue converter. A detailed description is given in the text.

the cleft closes completely, and the stereo-specific contacts are formed between myosin and actin. Loop 2 maintains its contact with the upper actin but releases the lower actin (Figure 6C). An unloaded single head of myosin V with bound ADP adopts a nearly postpower-stroke conformation, but this is not possible for the leading head in double-headed myosin V because it is tethered to the trailing head. Thus, the system is now under strain, consistent with images of myosin V attached to actin that show a bent appearance in the lever arm of the leading head (Walker et al., 2000). Processivity data provide evidence that attachment of the leading head accelerates ADP release from the rear head, thus favoring forward movement (Baker et al., 2004). The lever arm of the rear head undergoes a further, smaller displacement in the direction of movement upon ADP release. The leading head is still in the strained ADP position (Figure 6D). ATP binding to the trailing head causes the cleft in the motor domain to open, thus reducing myosin's affinity for actin, and causes loop 2 to rearrange to tether the trailing head to actin (Figure 6E). Because the tethering is relatively weak, the strain in the lead head triggers detachment

of the trailing head, allowing the strained lead head to execute its power stroke (Figure 6F). At the same time, the former trailing head gets thrust forward, hydrolyses ATP, and becomes the new leading head in a prepower-stroke conformation. After detachment from actin and initiation of hydrolysis, this head closes its cleft partially and exercises a reverse power stroke to form the detached transition state observed by crystallography for myosin II, ready to attach to the next binding site (Figures 6A and 6B).

It is noteworthy that we observe a single population for myosin V in the presence of ATP (lever down) but two populations for the attached transition (ADP.Pi) state (lever arm up or down). This observation implies that the detached head must hydrolyze ATP before it can become the new lead head with a prepower-stroke lever arm (Figures 6F to 6A transition). Moreover, the ability of the attached transition state to also adopt a postpower-stroke lever arm is likely a safeguard for maintaining processivity without back stepping in case the trail head hydrolyzes ATP while it is still attached to actin. This would allow the trailing head to remain attached to actin for a complete hydrolysis cycle without changing its lever arm position, thus maintaining the correct position for the leading head to seek the next actin binding site and continue processive movement.

Experimental Procedures

Protein Preparation

Chicken skeletal muscle actin was prepared and stored as described (Volkmann et al., 2000). It was generally used within 2–3 weeks of preparation. The murine myosin V construct consisting of the motor domain and two IQ binding motifs (MD2IQ) was truncated at amino acid 820, followed by a C-terminal FLAG epitope (DYKDDDDK) for affinity chromatography. Protein expression and purification is as described in Krementsov et al. (2004). The purified protein contained two bound calmodulins.

Actomyosin Complexes

Actin was diluted to ~0.05 mg/ml with 5 mM Imidazole (pH 7.5), 5 mM KCL, 2 mM $MgCl_2$, and 3 mM NaN_3 just prior to application to the glow-discharged 400-mesh copper grids coated with holey carbon film. After 1 min incubation in a humid chamber, the grids were rinsed twice with dilution buffer without the myosin but containing the relevant nucleotide (2 mM MgADP.AlF_4, 1 mM MgAMP-PNP, 1 mM MgADP, 1 mM MgATP, or no nucleotide for the apo state). Five microliters of MD2IQ was then incubated in nucleotide and was diluted to ~0.1 mg/ml in 10 mM Imidazole (pH 7.4), 10 mM NaCl, 1 mM $MgCl_2$, 1 mM EGTA, 1 mM DTT, 1 mM NaN_3, and nucleotide, applied to the grid for 30 s, and replaced by an additional drop of sample (30 s). The excess of liquid was blotted, and the grids were plunged into liquid ethane cooled by LN_2. ATP samples were freshly prepared in the cold room for each grid, and the MgATP was mixed with MD2IQ prior to application to the grid. MD2IQ was mixed with nucleotide at least 30 min prior to the experiment, except for ATP, which was mixed immediately prior to application to the grid.

Electron Microscopy

Low-dose images were recorded with a Tecnai 12 electron microscope (FEI Electron Optics) at a nominal magnification of 52,000× (at 120 keV) and ~1.5 μm defocus (electron dose ~10 $e^-/Å^2$). Micrographs were digitized with a SCAI scanner (Z/I Imaging Corporation) with a pixel size of 0.27 nm on the sample.

Helical Reconstruction

Helical reconstructions were obtained with the Brandeis Helical Package (Owen et al., 1996) as described (Volkmann et al., 2000). All reconstructions included 23 layer lines that were trimmed to 2.1 nm resolution. Because this resolution is within the first zero of the contrast transfer function, no phase correction was necessary. The abrupt edge that was introduced by this procedure was smoothed to zero by using a Gaussian falloff. Only layer lines that were found to be statistically significant in at least one of the individual filaments were used and included orders 2, –11, 4, –9, 6,–7, 8, –5, –3, –1, –12, 3, 14, 1, 5, –8, –4, –2, 7, –6, 13, and the equator. Individual filaments were reconstructed separately, aligned in real space (Hanein et al., 1997; Volkmann et al., 2000), normalized, and averaged. Quality indicators for the reconstructions are shown in Table 1.

Reconstruction by Iterative Helical Real Space Refinement

The iterative helical real space refinement method (Egelman, 2000) is a hybrid approach that uses real-space, single-particle processing and imposition of helical symmetry in an iterative manner. Our implementation uses EMAN (Ludtke et al., 1999) for the single-particle reconstruction portion and routines adapted from the CoAn suite (Volkmann and Hanein, 1999, 2003) to determine and impose the helical symmetry. This implementation was extensively tested with calculated and experimental data from frozen-hydrated actomyosin (see Supplemental Data). The first step of the procedure is the selection of overlapping boxes containing short helical segments. The optimal box size and overlap depend on several factors including desired resolution, signal-to-noise ratio, diameter of the helical structure, helical symmetry, and the homogeneity of the data set. A box size of 80 × 80 pixels with a 0.54 nm pixel size was used. This corresponds to about 15 asymmetric units of the helix, a little over one actin crossover. An overlap of 60 pixels was chosen, allowing every asymmetric unit to contribute to four different views of the helix.

Actin Modeling and Docking

An atomic model for filamentous actin based on rigid-body refinement against fiber diffraction data (Holmes et al., 2003) was docked into maps of undecorated actin (Volkmann et al., 2000) by using CoAn (Volkmann and Hanein, 1999). There were distinct density differences between the actin reconstructions and the model in the C-terminal region of the actin model. These differences were also present when the docked actin model was compared to maps of actin decorated with myosin or other actin binding proteins (Hanein et al., 1998), indicating a systematic mismatch between the model and the filament density. We modified the C-terminal region of actin to minimize these differences by using crosslinking constraints (Orlova et al., 2001) and stereochemistry as a guiding principle. After redocking the refined model into the reconstructions of undecorated actin, no further differences were observed. The accuracy of the docking was estimated by using two independent reconstructions and solution set analysis (Volkmann and Hanein, 1999, 2003).

Myosin Docking and Modeling

After real-space alignment (Hanein and DeRosier, 1999), the reconstruction of undecorated actin was subtracted from the respective myosin-V-decorated maps. Single units of the actin bound myosin-V densities were isolated with the watershed transform (Volkmann, 2002). Modular docking was used for the apo, ADP, and ATP reconstructions. The structure was divided into the motor domain (MD) and the two calmodulin chain regions. The relatively low resolution of the AMPPNP reconstruction did not permit modular docking, and an iterative refinement was used instead. At least two reconstructions for each type were used for crossvalidation throughout. For the MD docking, the available structures were divided into three groups. The postpower-stroke conformation was represented by pdb-entries 1MMA, 1MMN, 1MMD, 1MME, 2MYS, 1KK7, 1FMV, 1FMW, and 1W7J. The prepower-stroke conformation was represented by pdb-entries 1BR1, 1BR2, 1BR4, 1DFL, 1MND, and 1VOM. The third group contains the myosin V crystal structures with a similar lever arm position as the poststroke conformation but with a more tightly closed actin binding cleft in the absence of nucleotide and included the following: 1OE9, 1W8J (four asymmetric units), and 1W7I. The two bound calmodulins were modeled with the calmodulin-like essential light chain (LC1-sa) taken from

the myosin V crystal structure. Docking was done into discrepancy maps (see below) that had the MD portion removed. The initial placement of the first calmodulin was extrapolated from the docked crystal structure and then refined by using the refinement module from CoAn. After docking, the contribution of the first calmodulin model was removed from the map by discrepancy mapping and then the second calmodulin model was docked into the remainder without constraints. Regularization with REFMAC5 (Murshudov et al., 1997) was performed for all atomic models to relieve distortions in stereochemistry.

Discrepancy Mapping

In this technique, density is first calculated from the docked atomic model by using electronic scattering factors. Then, image-formation and image-analysis artifacts present in the reconstruction are compensated for by matching the Fourier amplitude spectrum of the calculated density to the observed one and by scaling the densities appropriately. Lastly, the modified density is subtracted voxel-wise from the observed reconstruction. The resulting discrepancy maps allow reliable localization of regions where the reconstruction has significantly more density than the model can explain. Through the use of multiple maps and crystal structures, an error estimate (standard deviation) for each voxel in the discrepancy maps can be calculated. This feature allows assignment of statistical significance. Peaks were considered significant if their value was at least three times their standard deviation.

Supplemental Data

Supplemental Data including three figures, one table, and four movies are available online with this article at http://www.molecule.org/cgi/content/full/19/5/595/DC1/.

Acknowledgments

We are indebted to Greta Ouyang for her involvement in the initial stages of this project. D.H. and N.V. thank Edward H. Egelman for providing his IHRS programs and David J. DeRosier (D.J.D.) for his support. This work was supported by National Institutes of Health Grants AR47199 to D.H., GM64473 to N.V., GM26357 to D.J.D., HL38113 to K.M.T., and AR47906 to S.L. and K.M.T.

Received: April 8, 2005
Revised: June 20, 2005
Accepted: July 14, 2005
Published: September 1, 2005

References

Baker, J.E., Krementsova, E.B., Kennedy, G.G., Armstrong, A., Trybus, K.M., and Warshaw, D.M. (2004). Myosin V processivity: multiple kinetic pathways for head-to-head coordination. Proc. Natl. Acad. Sci. USA *101*, 5542–5546. Published online March 31, 2004. 10.1073/pnas.0307247101.

Burgess, S.A., Walker, M.L., White, H.D., and Trinick, J. (1997). Flexibility within myosin heads revealed by negative stain and single-particle analysis. J. Cell Biol. *139*, 675–681.

Burgess, S., Walker, M., Wang, F., Sellers, J.R., White, H.D., Knight, P.J., and Trinick, J. (2002). The prepower stroke conformation of myosin V. J. Cell Biol. *159*, 983–991. Published online December 23, 2002. 10.1083/jcb.200208172.

Coureux, P.D., Wells, A.L., Menetrey, J., Yengo, C.M., Morris, C.A., Sweeney, H.L., and Houdusse, A. (2003). A structural state of the myosin V motor without bound nucleotide. Nature *425*, 419–423.

Coureux, P.D., Sweeney, H.L., and Houdusse, A. (2004). Three myosin V structures delineate essential features of chemo-mechanical transduction. EMBO J. *23*, 4527–4537.

De La Cruz, E.M., Wells, A.L., Rosenfeld, S.S., Ostap, E.M., and Sweeney, H.L. (1999). The kinetic mechanism of myosin V. Proc. Natl. Acad. Sci. USA *96*, 13726–13731.

De La Cruz, E.M., Wells, A.L., Sweeney, H.L., and Ostap, E.M. (2000). Actin and light chain isoform dependence of myosin V kinetics. Biochemistry *39*, 14196–14202.

Dominguez, R., Freyzon, Y., Trybus, K.M., and Cohen, C. (1998). Crystal structure of a vertebrate smooth muscle myosin motor domain and its complex with the essential light chain: visualization of the pre-power stroke state. Cell *94*, 559–571.

Egelman, E.H. (2000). A robust algorithm for the reconstruction of helical filaments using single-particle methods. Ultramicroscopy *85*, 225–234.

Fisher, A.J., Smith, C.A., Thoden, J.B., Smith, R., Sutoh, K., Holden, H.M., and Rayment, I. (1995). X-ray structures of the myosin motor domain of *Dictyostelium discoideum* complexed with MgADP.BeF_3 and MgADP.AlF_4. Biochemistry *34*, 8960–8972.

Galkin, V.E., Orlova, A., Lukoyanova, N., Wriggers, W., and Egelman, E.H. (2001). Actin depolymerizing factor stabilizes an existing state of F-actin and can change the tilt of F-actin subunits. J. Cell Biol. *153*, 75–86.

Galkin, V.E., Orlova, A., VanLoock, M.S., Rybakova, I.N., Ervasti, J.M., and Egelman, E.H. (2002). The utrophin actin-binding domain binds F-actin in two different modes: implications for the spectrin superfamily of proteins. J. Cell Biol. *157*, 243–251. Published online April 15, 2002. 10.1083/jcb.200111097.

Galkin, V.E., Orlova, A., VanLoock, M.S., and Egelman, E.H. (2003a). Do the utrophin tandem calponin homology domains bind F-actin in a compact or extended conformation? J. Mol. Biol. *331*, 967–972.

Galkin, V.E., Orlova, A., VanLoock, M.S., Shvetsov, A., Reisler, E., and Egelman, E.H. (2003b). ADF/cofilin use an intrinsic mode of F-actin instability to disrupt actin filaments. J. Cell Biol. *163*, 1057–1066. Published online December 1, 2003. 10.1083/jcb.200308144.

Gulick, A.M., Bauer, C.B., Thoden, J.B., and Rayment, I. (1997). X-ray structures of the MgADP, MgATPγS, and MgAMPPNP complexes of the *Dictyostelium discoideum* myosin motor domain. Biochemistry *36*, 11619–11628.

Hanein, D., and DeRosier, D. (1999). A new algorithm to align three-dimensional maps of helical structures. Ultramicroscopy *76*, 233–238.

Hanein, D., Matsudaira, P., and DeRosier, D.J. (1997). Evidence for a conformational change in actin induced by fimbrin (N375) binding. J. Cell Biol. *139*, 387–396.

Hanein, D., Volkmann, N., Goldsmith, S., Michon, A.M., Lehman, W., Craig, R., DeRosier, D., Almo, S., and Matsudaira, P. (1998). An atomic model of fimbrin binding to F-actin and its implications for filament crosslinking and regulation. Nat. Struct. Biol. *5*, 787–792.

Holmes, K.C., Angert, I., Kull, F.J., Jahn, W., and Schroder, R.R. (2003). Electron cryo-microscopy shows how strong binding of myosin to actin releases nucleotide. Nature *425*, 423–427.

Joel, P.B., Sweeney, H.L., and Trybus, K.M. (2003). Addition of lysines to the 50/20 kDa junction of myosin strengthens weak binding to actin without affecting the maximum ATPase activity. Biochemistry *42*, 9160–9166.

Krementsov, D.N., Krementsova, E.B., and Trybus, K.M. (2004). Myosin V: regulation by calcium, calmodulin, and the tail domain. J. Cell Biol. *164*, 877–886. Published online March 8, 2004. 10.1083/jcb.200310065.

Ludtke, S.J., Baldwin, P.R., and Chiu, W. (1999). EMAN: semiautomated software for high-resolution single-particle reconstructions. J. Struct. Biol. *128*, 82–97.

Lukoyanova, N., VanLoock, M.S., Orlova, A., Galkin, V.E., Wang, K., and Egelman, E.H. (2002). Each actin subunit has three nebulin binding sites: implications for steric blocking. Curr. Biol. *12*, 383–388.

Milligan, R.A. (1996). Protein-protein interactions in the rigor actomyosin complex. Proc. Natl. Acad. Sci. USA *93*, 21–26.

Moore, J.R., Krementsova, E.B., Trybus, K.M., and Warshaw, D.M. (2004). Does the myosin V neck act as a lever? J. Muscle Res. Cell Motil. *25*, 29–35.

Murshudov, G.N., Vagin, A.A., and Dodson, E.J. (1997). Refinement of macromolecular structures by the maximum-likelihood method. Acta. Crystallogr. D Biol. Crystallogr. *53*, 240–255.

Orlova, A., Galkin, V.E., VanLoock, M.S., Kim, E., Shvetsov, A., Reisler, E., and Egelman, E.H. (2001). Probing the structure of F-actin: cross-links constrain atomic models and modify actin dynamics. J. Mol. Biol. *312*, 95–106.

Orlova, A., Shvetsov, A., Galkin, V.E., Kudryashov, D.S., Rubenstein, P.A., Egelman, E.H., and Reisler, E. (2004). Actin-destabilizing factors disrupt filaments by means of a time reversal of polymerization. Proc. Natl. Acad. Sci. USA *101*, 17664–17668. Published online December 10, 2004. 10.1073/pnas.0407525102.

Owen, C.H., Morgan, D.G., and DeRosier, D.J. (1996). Image analysis of helical objects: the Brandeis Helical Package. J. Struct. Biol. *116*, 167–175.

Rayment, I., Holden, H.M., Whittaker, M., Yohn, C.B., Lorenz, M., Holmes, K.C., and Milligan, R.A. (1993a). Structure of the actin-myosin complex and its implications for muscle contraction. Science *261*, 58–65.

Rayment, I., Rypniewski, W.R., Schmidt-Base, K., Smith, R., Tomchick, D.R., Benning, M.M., Winkelmann, D.A., Wesenberg, G., and Holden, H.M. (1993b). Three-dimensional structure of myosin subfragment-1: a molecular motor. Science *261*, 50–58.

Rost, L.E., Hanein, D., and DeRosier, D.J. (1998). Reconstruction of symmetry deviations: a procedure to analyze partially decorated F-actin and other incomplete structures. Ultramicroscopy *72*, 187–197.

Taylor, K.A., Schmitz, H., Reedy, M.C., Goldman, Y.E., Franzini-Armstrong, C., Sasaki, H., Tregear, R.T., Poole, K., Lucaveche, C., Edwards, R.J., et al. (1999). Tomographic 3D reconstruction of quick-frozen, Ca2+-activated contracting insect flight muscle. Cell *99*, 421–431.

Vale, R.D. (2003). Myosin V motor proteins: marching stepwise towards a mechanism. J. Cell Biol. *163*, 445–450.

Volkmann, N. (2002). A novel three-dimensional variant of the watershed transform for segmentation of electron density maps. J. Struct. Biol. *138*, 123–130.

Volkmann, N., and Hanein, D. (1999). Quantitative fitting of atomic models into observed densities derived by electron microscopy. J. Struct. Biol. *125*, 176–184.

Volkmann, N., and Hanein, D. (2000). Actomyosin: law and order in motility. Curr. Opin. Cell Biol. *12*, 26–34.

Volkmann, N., and Hanein, D. (2003). Docking of atomic models into reconstructions from electron microscopy. Methods Enzymol. *374*, 204–225.

Volkmann, N., Hanein, D., Ouyang, G., Trybus, K.M., DeRosier, D.J., and Lowey, S. (2000). Evidence for cleft closure in actomyosin upon ADP release. Nat. Struct. Biol. *7*, 1147–1155.

Volkmann, N., Ouyang, G., Trybus, K.M., DeRosier, D.J., Lowey, S., and Hanein, D. (2003). Myosin isoforms show unique conformations in the actin-bound state. Proc. Natl. Acad. Sci. USA *100*, 3227–3232. Published online February 28, 2003. 10.1073/pnas.0536510100.

Walker, M.L., Burgess, S.A., Sellers, J.R., Wang, F., Hammer, J.A., 3rd, Trinick, J., and Knight, P.J. (2000). Two-headed binding of a processive myosin to F-actin. Nature *405*, 804–807.

Whittaker, M., Wilson-Kubalek, E.M., Smith, J.E., Faust, L., Milligan, R.A., and Sweeney, H.L. (1995). A 35Å movement of smooth muscle myosin on ADP release. Nature *378*, 748–751.

Yang, S., Yu, X., Galkin, V.E., and Egelman, E.H. (2003). Issues of resolution and polymorphism in single-particle reconstruction. J. Struct. Biol. *144*, 162–171.

Yengo, C.M., and Sweeney, H.L. (2004). Functional role of loop 2 in myosin V. Biochemistry *43*, 2605–2612.

Yengo, C.M., De la Cruz, E.M., Safer, D., Ostap, E.M., and Sweeney, H.L. (2002). Kinetic characterization of the weak binding states of myosin V. Biochemistry *41*, 8508–8517.